Study of broadband polarization conversion with metallic surface-relief gratings by rigorous coupled-wave analysis

Chang-Ching Tsai* and Shin-Tson Wu

College of Optics and Photonics, University of Central Florida, Orlando, Florida 32816, USA
**Corresponding author: tsaicc@creol.ucf.edu*

Received January 8, 2008; revised April 2, 2008; accepted April 2, 2008;
posted April 8, 2008 (Doc. ID 91387); published May 16, 2008

The conical rigorous coupled-wave analysis (RCWA) is employed to calculate the polarization conversion through the excitation of surface plasmons on metallic gratings. Various examples are examined with this numerical scheme. Our calculated results are consistent with those obtained from experiment and from other numerical methods. Three types of subwavelength surface-relief gratings are studied for the capability of broadband polarization conversion in the visible region. For wide-angle applications, various incident angles are studied and high polarization conversion efficiency is achieved. © 2008 Optical Society of America

OCIS codes: 050.1950, 050.1755, 240.6680, 260.5430.

1. INTRODUCTION

Polarization conversion (PC) of incident light by metallic gratings has been studied extensively. The early experiment of Bryan-Brown and Sambles demonstrated certain degrees of polarization rotation of the reflected light via excitation of surface plasmons on a silver-coated grating [1]. The broken surface symmetry that results in the rotation of the polarization plane is actually due to conical diffraction with azimuthal angle neither parallel nor normal to the grating vector [2]. To obtain large conversion efficiency, it relies on the surface plasmons excited in high-aspect-ratio metallic gratings. More detailed analysis on such surface plasmon resonance coupled with incident light of different polarizations can be found in the literature [3–7].

For a long time, PC by several profiles of metal-stripe or metallic surface gratings has been discussed only for monochromatic light. Recently, two respective types of Gaussian ridge and rectangular surface-relief gratings that enable broadband polarization conversion (BPC) in the visible and microwave regions have been reported [8–10]. Such a BPC optical element would be much appreciated in many optical devices whenever polarization rotation is demanded.

Many researchers have modeled the light with metallic gratings based on the differential formalism developed by Chandezon *et al.* [11], which solves the Maxwell equations with the technique of straightening grating profiles by nonorthogonal curvilinear coordinate transformation. Others have used Yasuura's method [12,13], a mode-matching method with finite truncated series, to calculate the *p-s* (TM-TE) mode conversion by metallic gratings and obtained results quite consistent with experiment [14].

Another common approach is the conical rigorous coupled-wave analysis (RCWA) proposed by Moharam *et al.* [15,16] or the rigorous Fourier modal method suggested by Li [17], both of which have been successfully adapted to the design of subwavelength PC gratings [10,18,19]. In the present work, we will use RCWA to calculate PC including broadband application with highly reflective metallic gratings. We have found in this work that with separation of *s* and *p* modes in the choice of reference coordinate, it is feasible to obtain PC by means of RCWA calculation.

In previous studies of metallic gratings, although nonnormal incident angles for monochromatic PC have been discussed, for cases of achromatic wave, only single-incident-angle light was considered. Here we further investigate PC with variation of incident angle for application to broadband and wide-angle illumination sources. This wide-angle analysis is practically beneficial, since for finite sizes of optical waves, such as Gaussian beams, the propagation of the Fourier wave vectors diverge in different propagating directions.

Because the angle is not limited to normal incidence, we also investigate the maximum PC condition with various conical mounting conditions. We show that the optimal azimuthal angle is not necessarily 45°. This numerical result would extend the optimized azimuthal condition for shallow gratings reported by Depine and Lester [20] to deep gratings. Besides the Gaussian ridge profile proposed in [8], we also discuss two particular structures of rectangular and trapezoidal gratings that are capable of converting polarization both over broad bandwidth and wide incidence angles. In addition, the shift of the peak PC in the wavelength spectrum with respect to the grating pitch will be illustrated.

Also, in considering a real situation, experimental dispersion data of the refractive index of metallic grating in visible wavelengths are used in our calculation. Although there are choices of metallic gratings, here only the results with silver gratings are presented. Moreover, for control of beam quality and effective rotation of polariza-

tion, the subwavelength metallic grating is the main subject we will discuss to ensure the zeroth diffraction order is the only nonevanescent harmonic that carries the power flow.

The organization of this paper is as following. In Section 2, we will review the conical RCWA theory and show how we calculate the PC. The validity of the applicability of RCWA is confirmed with examples in Section 3, including several grating profiles for achromatic PC. The accordingly optimized incidence parameters for broadband PC are illustrated with numerical results as well. In Section 4, we summarize our work and consider possible future work.

2. MODELING POLARIZATION CONVERSION BY RIGOROUS COUPLED-WAVE THEORY

In the modeling of polarization conversion, a detailed analytical result [21] was given with Rayleigh's field expansion in shallow metallic grating. However, it is not applicable to the present gratings because of the limit of its small groove depth approximation $d \ll \Lambda$, where the pitch Λ is about the same order of wavelength λ. As mentioned in [8], for broadband polarization conversion, the groove depth is about one quarter of the wavelength, $d \approx \lambda/4$. In such cases, the excitation and coupling of surface plasmons with the incident and diffracted light are quite complicated, and numerical schemes were needed to attain the solution of diffracted waves.

For calculation of diffraction gratings, there are two categories classified as differential and integral methods [22]. In the differential method, in spite of previous Chandezon's or Yasuura's results, RCWA has been one of the most widely used approaches. Although RCWA has been used to calculate the PC for dielectric and metallic gratings by other researchers, here we will apply RCWA to highly reflective metallic gratings in separate equivalent TE and TM boundary conditions and address the convergence formulation as follows.

In early formulations of RCWA for metallic surface-relief gratings, the problem was encountered of slow convergence in expanding the diffraction orders for the TM wave [23]. This drawback soon was improved for deep gratings as suggested by Lalanne and Morris [24], and Granet and Guizal [25]. However, for shallow gratings, the classical (Moharam) method proved to have better convergence performance [26]. Later, to the best of our knowledge, a convergent scheme suggested by Popov and Neviére [27] based on Li's factorization rule [28] has shown proficiency in fast convergence. However, all the previously published results were concerned mainly with the diffraction efficiency, not polarization rotation. In calculating PC by RCWA, the abovementioned schemes still encounter certain convergence problems in different grating profiles. This was recently observed by the authors and a new method was proposed to improve the convergence. Here we adopt this new method to calculate the conical metallic diffraction, and the results consistent with experimental and other approaches will be given.

Simply speaking, the nature of polarization conversion is a consequence of relative phase difference of s and p components (fast and slow modes) in highly reflective gratings [3]. These modes and surface plasmon polaritons are coupled in a very complicated way to enhance or suppress PC, a process that is critically dependent on the grating structure and orientation. Therefore, in studying these modes' interactions with metallic gratings, the spherical coordinate is preferred in the conical mounting analysis, to include all the decisive parameters, the incidents polar and azimuthal angles, and the grating orientation.

With the above considerations, it is convenient to coordinate the normalized incident field $\boldsymbol{E}_{inc}$ of arbitrary unit wavevector $\mathbf{k}$ and polarization $\mathbf{u}$ in region $\mathbf{I}$ as

$$\boldsymbol{E}_{inc} = \mathbf{u} \exp[-jk_0 n_I (x \sin\theta \cos\phi + y \sin\theta \sin\phi + z \cos\theta)]. \tag{1}$$

The unit polarization vector $\mathbf{u}$ is

$$\mathbf{u} = (\sin\psi \sin\phi - \cos\psi \cos\theta \cos\phi)\mathbf{x} - (\sin\psi \cos\phi + \cos\psi \cos\theta \sin\phi)\mathbf{y} + (\cos\psi \sin\theta)\mathbf{z}, \tag{2}$$

where θ is the polar (incidence) angle, ϕ is the azimuthal angle, and ψ is the polarization angle (the angle between $\mathbf{u}$ and $\mathbf{j}$ in the incident plane Γ, where the unit normal vector $\mathbf{i}$ and tangential vector $\mathbf{j}$ with respect to Γ satisfy $\mathbf{i} \times \mathbf{j} = \mathbf{k}$) as illustrated in Fig. 1(a). The grating is in the $\mathbf{x}$-$\mathbf{y}$ plane with the grating vector along $\mathbf{x}$, and the incidence plane Γ is determined by the $\mathbf{k}$ and $\mathbf{z}$ vectors. With $\psi = 0°$ or 90° $\mathbf{u}$ corresponds to the $\boldsymbol{H}$ or $\boldsymbol{E}$ field that is perpendicular to the plane of incidence, respectively.

An advantage of the polarization angle ψ is that we can assign the equivalent p (TM) wave as $\psi = 0°$ or the s (TE) wave as $\psi = 90°$. When $\psi = 90°$ $\mathbf{u}$ has x and y components only, which means the polarization is tangential to the grating plane. Such decomposition of the equivalent p, s waves in the reference frame of the incidence plane can immediately enable us to use the boundary conditions obtained from nonconical cases. More important, it turns out to be a convenient way to calculate the PC, as shown later.

Here we will follow Moharam's staircase approximation for continuous surface gratings. The normalized reflected electric (magnetic) field $\boldsymbol{E}(\boldsymbol{H})_{\mathrm{R}}$ in region $\mathbf{I}$ $(z > 0)$, the transmitted field $\boldsymbol{E}(\boldsymbol{H})_{\mathrm{T}}$ in region $\mathbf{II}$ $(z > d)$, and the Floquet waves $\boldsymbol{E}(\boldsymbol{H})_{\mathrm{G}}$ in groove region $\mathbf{III}$ $(d > z > 0)$ of several slices shown in Fig. 1(b) are designated as

$$\boldsymbol{E}(\boldsymbol{H})_{\mathrm{R}} = \sum_i \boldsymbol{E}(\boldsymbol{H})_{\mathrm{R}i} \exp[-j(k_{xi}x + k_{yi}y + k_{\mathbf{I},zi}z)], \tag{3}$$

$$\boldsymbol{E}(\boldsymbol{H})_{\mathrm{T}} = \sum_i \boldsymbol{E}(\boldsymbol{H})_{\mathrm{T}i} \exp[-jk_{xi}x + k_{yi}y + k_{\mathbf{II},zi}(z-d)], \tag{4}$$

$$\boldsymbol{E}_{\mathrm{G}} = \sum_i \boldsymbol{S}(z)_i \exp[-j(k_{xi}x + k_{yi}y)], \tag{5}$$

$$\boldsymbol{H}_{\mathrm{G}} = -j(\varepsilon_0/\mu_0) \sum_i \boldsymbol{U}(z)_i \exp[-j(k_{xi}x + k_{yi}y)], \tag{6}$$

where $k_{xi} = k_0 n_{\mathbf{I}} \sin\theta \cos\phi - i \cdot 2\pi/\Lambda$ and $k_y = k_0 n_{\mathbf{I}} \sin\theta \sin\phi$ with diffracted order i and grating period Λ; $k_{\mathbf{I(II)},zi} = [(k_0 n_{\mathbf{I(II)}})^2 - k_{xi}^2 - k_{yi}^2]^{1/2}$ if $\mathrm{Im}[k_{\mathbf{I(II)},zi}] \le 0$ and

$k_{\mathbf{I(II)},zi}=-[(k_0 n_{\mathbf{I(II)}})^2-k_{xi}^2-k_{yi}^2]^{1/2}$ if $\mathrm{Im}[k_{\mathbf{I(II)},zi}]>0$ and the sign of the imaginary part is adopted for evanescent waves.

Substituting Eqs. (5) and (6) into the Maxwell equations, and matching the tangential fields on each slice of the gratings, we have the wave equations

$$\frac{\mathrm{d}}{\mathrm{d}z'}\begin{bmatrix}\mathbf{S}_y\\ \mathbf{S}_x\\ \mathbf{U}_y\\ \mathbf{U}_x\end{bmatrix}=\begin{bmatrix}0 & 0 & \mathbf{K}_y\mathbf{Q}_{zz}^{-1}\mathbf{K}_x & -\mathbf{K}_y\mathbf{Q}_{zz}^{-1}\mathbf{K}_y+\mathbf{I}\\ 0 & 0 & \mathbf{K}_x\mathbf{Q}_{zz}^{-1}\mathbf{K}_x-\mathbf{I} & -\mathbf{K}_x\mathbf{Q}_{zz}^{-1}\mathbf{K}_y\\ \mathbf{K}_y\mathbf{K}_x & -\mathbf{K}_y^2+\mathbf{Q}_{xx} & 0 & 0\\ \mathbf{K}_x^2-\mathbf{Q}_{yy} & -\mathbf{K}_x\mathbf{K}_y & 0 & 0\end{bmatrix}\begin{bmatrix}\mathbf{S}_y\\ \mathbf{S}_x\\ \mathbf{U}_y\\ \mathbf{U}_x\end{bmatrix}, \tag{7}$$

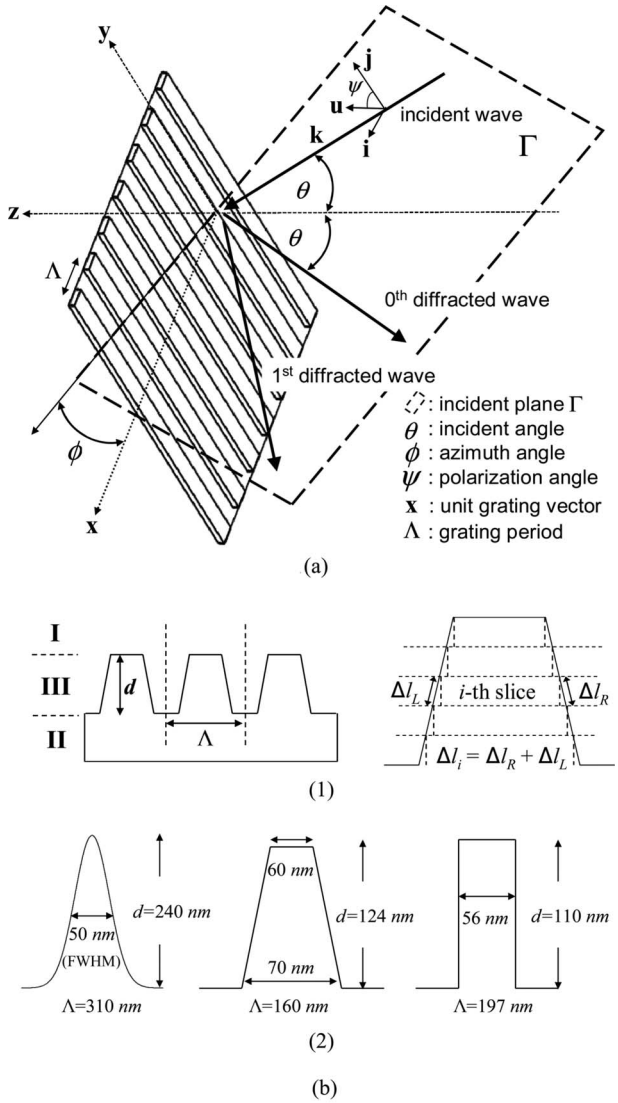

Fig. 1. (a) Configuration of conical diffraction by one-dimensional surface-relief grating with incident angle θ, azimuthal angle ϕ, polarization angle ψ, and grating period Λ. (b) (1) Three regions of RCWA for light incident from medium **I** into medium **II** with coupled wave in groove region **III** and the staircase approximation for continuous surface-relief gratings, where Δl_i is the sum of two segments on each side of slice i. (2) Three grating profiles that enable broadband R_{ps}^0: the Gaussian ridge, the trapezoidal, and the binary grating. Their corresponding $R_{ps}^0(\lambda)$ are shown in Fig. 6.

where the elements in the dielectric Q_ε tensor are written as

$$\mathrm{Q}_\varepsilon=\begin{bmatrix}\mathbf{Q}_{xx} & 0 & 0\\ 0 & \mathbf{Q}_{yy} & 0\\ 0 & 0 & \mathbf{Q}_{zz}\end{bmatrix}=\begin{bmatrix}\mathrm{n}_z^2\mathbf{E}+\mathrm{n}_x^2\mathbf{A}^{-1} & 0 & 0\\ 0 & \mathbf{E} & 0\\ 0 & 0 & \mathrm{n}_x^2\mathbf{E}+\mathrm{n}_z^2\mathbf{A}^{-1}\end{bmatrix}. \tag{8}$$

The matrices $\mathbf{K}_x$, $\mathbf{K}_y$, $\mathbf{A}$, and $\mathbf{E}$ are notations defined in [15], where $\mathbf{K}_{x(y)}$ is a diagonal matrix with the (i,i) element being $k_{x(y)i}/k_0$, $\mathbf{E}$ is the Toeplitz matrix of the permittivity harmonic components, $\mathbf{A}=\mathbf{K}_x^2-\mathbf{E}$, and $z'=k_0 z$. The matrix coefficients n_x and n_z are the x and z components of the normal unit vector $\mathbf{n}$ at each slice on the grating surface satisfying $\mathrm{n}_x^2+\mathrm{n}_z^2=1$.

The introduction of the Q_ε tensor is to improve the convergence, which is different from the formulation in [27]. The Q_ε tensor proposed by Popov and Neviére according to Li's factorization rule contains the elements of Toeplitz matrices $[[\mathrm{n}_x^2]]$, $[[\mathrm{n}_z^2]]$, and $[[\mathrm{n}_x\mathrm{n}_z]]$; we will not discuss this in too much detail here. The construction of each Toeplitz matrix is described in [27]. Instead of using the Toeplitz matrix, our n_{xi}^2, n_{zi}^2 for each slice i of the grating profile in the staircase approximation are defined as

$$\mathrm{n}_{xi}^2=\frac{\int_{\Delta l_i}\mathrm{n}_x^2(p)\mathrm{d}l_i}{\Delta l_i},$$

$$\mathrm{n}_{zi}^2=\frac{\int_{\Delta l_i}\mathrm{n}_z^2(p)\mathrm{d}l_i}{\Delta l_i}, \tag{9}$$

where p is the integrated point on the surface segment of each slice of the grating; $\mathrm{n}_{xi}^2(p)$, $\mathrm{n}_{zi}^2(p)$ are the squares of the x and z components of unit vector $\mathbf{n}(p)$ normal to the surface, and Δl_i [see Fig. 1(b)] is the total length of the sum of two segments on each side of slice i associated with its line integral element $\mathrm{d}l_i$. This new formulation will prove its validity by the various examples presented

in Section 3. Indeed, our convergence scheme is based on the physics inspired by Rayleigh's diffraction integral. The postulation, explanation, and derivation of Eqs. (8) and (9), together with their convergence performance compared with other methods, will be addressed elsewhere [29].

Equation (7) can be further simplified into a set of two second-order differential equations as

$$\frac{d^2}{dz'^2}\begin{bmatrix}\mathbf{S}_y\\ \mathbf{S}_x\end{bmatrix}=\begin{bmatrix}\mathbf{K}_y\mathbf{Q}_{zz}^{-1}\mathbf{K}_y\mathbf{Q}_{yy}+\mathbf{K}_x^2-\mathbf{Q}_{yy} & \mathbf{K}_y\mathbf{Q}_{zz}^{-1}\mathbf{K}_x\mathbf{Q}_{xx}-\mathbf{K}_x\mathbf{K}_y\\ \mathbf{K}_x\mathbf{Q}_{zz}^{-1}\mathbf{K}_y\mathbf{Q}_{yy}-\mathbf{K}_y\mathbf{K}_x & \mathbf{K}_x\mathbf{Q}_{zz}^{-1}\mathbf{K}_x\mathbf{Q}_{xx}-\mathbf{Q}_{xx}\end{bmatrix}\begin{bmatrix}\mathbf{S}_y\\ \mathbf{S}_x\end{bmatrix}. \tag{10}$$

The Floquet waves $\boldsymbol{U}_y$ and $\boldsymbol{U}_x$ can be easily obtained by the eigensolutions of Eq. (7) through coupled wave equations. Now care in the choices of matching boundary conditions in the upper and lower bounds of groove region is essential. As indicated earlier, we will use the incidence plane as a new reference frame by rotating each azimuthal angle ϕ_i of every reflection (transmission) field $\boldsymbol{E}(\boldsymbol{H})_{\mathrm{R(T)}i}$ about the z axis onto it. Here the rotation angle is $\phi_i=\tan^{-1}(k_y/k_{xi})$. The new reflected and transmitted electric fields are represented as $\boldsymbol{E}'_{\mathrm{R(T)}}=\boldsymbol{E}'_{\mathrm{R(T)},\tan,i}+E'_{\mathrm{R(T)},zi}\mathbf{z}$. The tangential vectors are $\mathbf{E}'_{\mathrm{R(T)},\tan,i}=E_{\mathrm{R(T)}\parallel i}\mathbf{t}+E_{\mathrm{R(T)}\perp i}\mathbf{n}$ with the unit vectors $\mathbf{t}$ and $\mathbf{n}$, respectively parallel and perpendicular to the incident plane satisfying $\mathbf{t}\times\mathbf{n}=\mathbf{z}$. The z components remain the same, i.e., $E'_{\mathrm{R(T)},zi}=E_{\mathrm{R(T)},zi}$.

The new $\boldsymbol{E}'_{\mathrm{R(T)},\tan,i}$ are related to the old $\boldsymbol{E}_{\mathrm{R(T)},\tan,i}$ by Euler rotation matrix $R(\phi_i)=\begin{bmatrix}\cos\phi_i & \sin\phi_i\\ -\sin\phi_i & \cos\phi_i\end{bmatrix}$. Namely,

$$\begin{bmatrix}E_{\mathrm{R(T)}\parallel i}\\ E_{\mathrm{R(T)}\perp i}\end{bmatrix}=[R(\phi_i)]\begin{bmatrix}E_{\mathrm{R(T)}xi}\\ E_{\mathrm{R(T)}yi}\end{bmatrix}. \tag{11}$$

To completely match the boundary conditions also requires the rotation of tangential $\boldsymbol{S}_i$ and $\boldsymbol{U}_i$ waves. This will result in the coupling of the two components of eigenvectors $\boldsymbol{S}(\boldsymbol{U})_{xi}$ and $\boldsymbol{S}(\boldsymbol{U})_{yi}$ in the new boundary equations. Let us further express the parallel electric fields $E_{\mathrm{R(T)}\parallel i}$ in terms of the respective normal and z-component magnetic fields $(H_{\mathrm{R(T)}\perp i},H_{\mathrm{R(T)}zi})$ and the parallel magnetic fields $H_{\mathrm{R(T)}\parallel i}$ in terms of the respective normal and z-component electric fields $(E_{\mathrm{R(T)}\perp i},E_{\mathrm{R(T)}zi})$ from the Maxwell equations accordingly as

$$E_{\mathrm{R(T)}\parallel i}=\mp\sqrt{\frac{\mu_0}{\varepsilon_0}\left(\frac{k_{\mathbf{I(II)},zi}}{k_0 n_{\mathbf{I(II)}}^2}\right)}H_{\mathrm{R(T)}\perp i},$$

$$H_{\mathrm{R(T)}\parallel i}=\pm\sqrt{\frac{\varepsilon_0}{\mu_0}\left(\frac{k_{\mathbf{I(II)},zi}}{k_0}\right)}E_{\mathrm{R(T)}\perp i}. \tag{12}$$

The absence of the z components $E(H)_{\mathrm{R(T)},zi}$ in Eq. (12) is due to the zero normal components of wave vectors $k_{\mathrm{R(T)}\perp i}=0$ since we are in the incidence-plane reference frame. As a result, with substitution of Eq. (12) the new boundary equations of $\boldsymbol{S}(\boldsymbol{U})_{x,yi}$ and $\boldsymbol{E}(\boldsymbol{H})_{\mathrm{R(T)}i}$ contain only the normal electric and magnetic fields $E(H)_{\mathrm{R(T)}\perp i}$. Solving these new coupled equations at $z=0$ and $z=d$ for the undetermined coefficients of the eigensolutions of $\boldsymbol{S}(\boldsymbol{U})_{x,yi}$, we can then obtain the solution of $H_{\mathrm{R(T)}\perp i}$ and $E_{\mathrm{R(T)}\perp i}$ from the determined coefficients. Readers can find the detailed description in [15]. Since no propagation mode of high plasma frequency exists inside the metal, we discuss only the reflective propagation waves. In this way, the reflection diffraction efficiency $\mathrm{DE}_{\mathrm{R}i}$ is defined as

$$\mathrm{DE}_{\mathrm{R}i}=|E_{\mathrm{R}\perp i}|^2\mathrm{Re}\left(\frac{k_{\mathbf{I},zi}}{k_0 n_{\mathbf{I}}\cos\theta}\right)+|H_{\mathrm{R}\perp i}|^2\mathrm{Re}\left(\frac{k_{\mathbf{I},zi}/n_{\mathbf{I}}^2}{k_0 n_{\mathbf{I}}\cos\theta}\right), \tag{13}$$

where we take the real part of $k_{\mathbf{I},zi}$ for the propagating modes.

By examining Eq. (13) carefully, we find the advantage of coordinate decomposition through Eq. (11) and field substitution through Eq. (12). First, the diffraction efficiency in fact is the normalized total power across the x-y plane contributed by all polarization amplitudes, which now are completely represented by $E(H)_{\mathrm{R}\perp i}$. This is the result of the choice of reference frame.

Second, by the principle of superposition $E_{\mathrm{R}\perp i}$ represents the amplitude of the reflective equivalent-TE wave component, and $H_{\mathrm{R}\perp i}$ represents the amplitude of the reflective equivalent-TM wave component. Here we emphasize again that the equivalent TE or TM waves are defined with respect to the incident plane.

Third, if we choose the normalized incident light to be TE polarization, i.e., $\psi=90°$ in Eq. (2), the resultant value of $|H_{\mathrm{R}\perp i}|^2\mathrm{Re}(k_{\mathbf{I},zi}/k_0 n_{\mathbf{I}}^3\cos\theta)$ in Eq. (13) is the power carried by the TM component of reflective light in the z direction. This means for an incident TE wave, if we have a nonzero TM part of the reflective wave, then the polarization has been rotated. In the case of zero reflective normal electric field, i.e., $E_{\mathrm{R}\perp i}=0$, for TE incident light, then we have total PC. Here we follow the convention in literature and designate the normalized polarization-converted term in Eq. (13) as the PC efficiency: $R_{ps}=\Sigma_i|E_{\mathrm{R}\perp i}|^2\mathrm{Re}(k_{\mathbf{I},zi}/k_0 n_{\mathbf{I}}\cos\theta)$ for incident p wave converted into s wave and $R_{sp}=\Sigma_i|H_{\mathrm{R}\perp i}|^2\mathrm{Re}(k_{\mathbf{I},zi}/k_0 n_{\mathbf{I}}^3\cos\theta)$ for incident $s$wave converted into p wave. The ratio between the converted and original polarization fraction in Eq. (13) with summation over i can define the degree of polarization rotation.

One can further verify that the polarization conversion is due to the broken surface symmetry by Eq. (13). Set the incident azimuthal angle $\phi=0°$ or 90° for an incident s light; the resultant p wave is always zero $H_{\mathrm{R}\perp i}=0$, i.e., when the incident polarization is parallel or normal to the grating vector, there is no PC. This is the case of nonbroken surface symmetry. And for shallow surface grating,

$d \ll \Lambda$, Eq. (13) also gives the correct result that the maximum PC occurs when the azimuthal angle is at $\phi = 45°$.

Another feature of PC through metallic gratings is the property of reciprocity [18,21,30]. That is, for the same incident configuration, the conversion efficiency of the zeroth diffracted order from incident s wave into reflective p wave is the same as from incident p wave into reflective s wave; in other words, $R_{ps}^0 = R_{sp}^0$. We can tell that Eq. (13) supports this reciprocity relation well, and all the features mentioned above will be numerically illustrated in the next section.

3. NUMERICAL EXAMPLES OF PC WITH METALLIC GRATINGS

In this section, we show some numerical results of PC conversion using Eq. (13) implemented with our convergence formulation Eqs. (8) and (9). Several important characteristics of PC will be examined thoroughly. The first demonstration is the R_{ps}^0 as a function of θ for a shallow sinusoidal silver grating with fixed $\phi = 45°$, as shown in Fig. 2. We can see that the maximum $R_{ps}^0 = 0.089$ occurs at $\theta = 18.08°$, which is consistent both with the experimental and theoretical results given in [2].

Figure 3(a) shows another property: that the maximum R_{ps}^0 occurs at $\phi = 45°$ and is zero at $\phi = 0°$ or 90°, which also coincides with the result in [2]. Figure 3(b) is the corresponding incident angle θ-to-ϕ function for the maximum $R_{ps}^0(\phi, \theta)$ found. Also the square–cross curve shown in Fig. 3(a) verifies the reciprocity property: It is clear that the R_{ps}^0 curve is identical to that of R_{sp}^0.

Another nontrivial feature is if we increase the groove depth d then the maximum R_{ps}^0 will be greatly enhanced. This is because a higher-modulated grating receives more of the normal (to the surface) component of the E field, which induces more surface charges and generates stronger surface plasmon waves. However, if the depth exceeds a certain value, the R_{ps}^0 induced by the surface plasmon wave may decrease. Here we use RCWA to confirm this effect as shown in Fig. 4, which is consistent with the experimental result reported in [1] within the range of groove depth $0 < d < 95$ nm. We see that when $d \approx 95$ nm the R_{ps}^0 starts to decrease but rises again at $d \approx 110$ nm. Readers should keep in mind that although the depth of grating increases, the shallow grating condition $d \ll \Lambda$ still holds. More details regarding the mechanism of maximum R_{ps}^0 will be discussed in the following.

In the next example, we use RCWA to recalculate the broadband R_{ps}^0 in the visible region with the deep grating suggested in [8]. As indicated there, the numerical result of a silver Gaussian-ridge grating of 50 nm width (FWHM), 240 nm height and 250 nm period was shown to

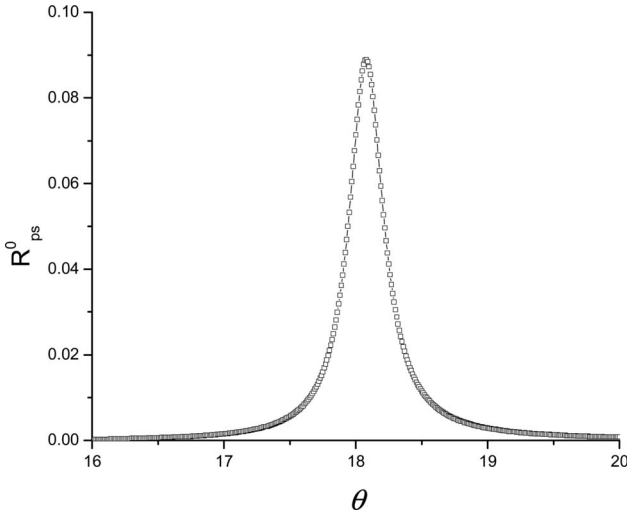

Fig. 2. R_{ps}^0 of incident angle θ at azimuthal angle $\phi = 45°$ for a shallow sinusoidal silver grating of $\varepsilon = -16 + 0.71i$, $\Lambda = 800.8$ nm, $d = 25.2$ nm, and $\lambda = 632.8$ nm, which is consistent with both the experimental and theoretical results given in Fig. 2 of [2]. The maximum $R_{ps}^0 = 0.089$ occurs at $\theta = 18.08°$.

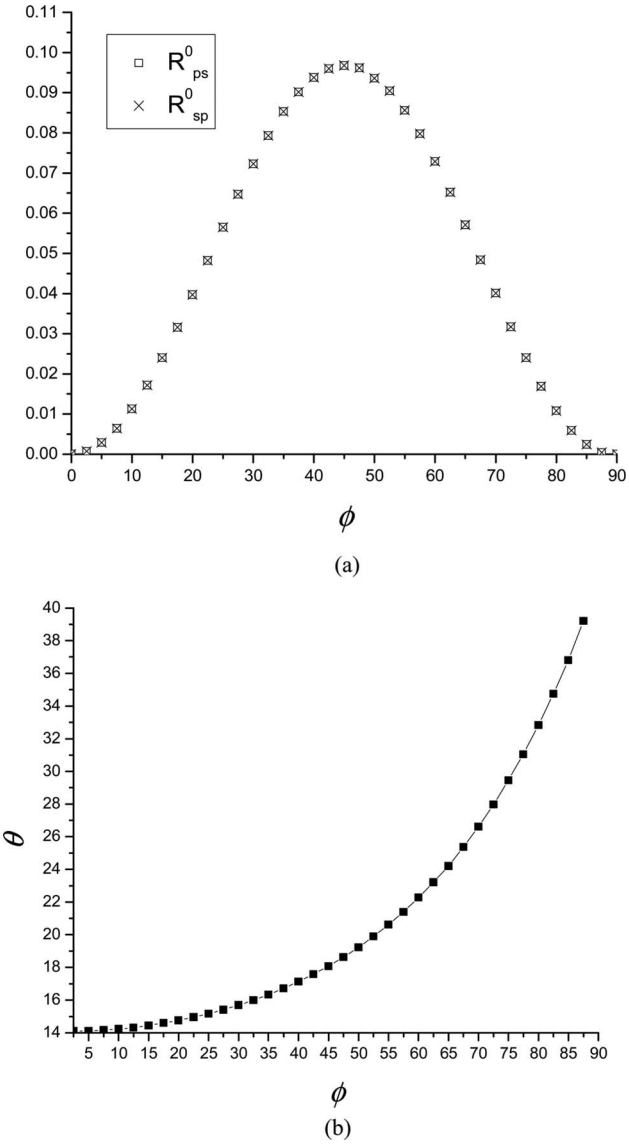

Fig. 3. (a) Maximum R_{ps}^0 for various ϕ with the same grating profile in of Fig. 2. The peak maximum R_{ps}^0 occurs at $\phi = 45°$ and is zero at $\phi = 0°$ or 90°, which coincides with the Fig. 3 in [2]. The conversion efficiency follows the square rule of a sinusoidal function, $R_{ps}(\theta, \phi) \propto \sin^2(2\phi)$ [1,21]. The curve of squares for the conversion from p to s and that of crosses for s to p conversion under the same incidence conditions clearly coincide. (b) Corresponding incidence angle θ to ϕ for the maximum $R_{ps}^0(\phi, \theta)$.

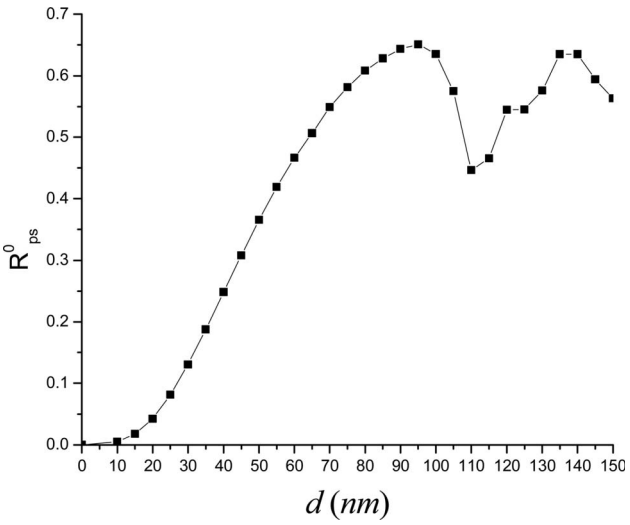

Fig. 4. Maximum R^0_{ps} of the groove depth d ranging from 0 to 150 nm with the same grating profile as Fig. 2, but here $\Lambda=842.5$ nm. The portion of d from 0 to 90 nm in this figure is consistent with the experimental result in Fig. 4 of [1]. The peak of $R^0_{ps}(d)=0.65$ occurs at $d=95$ nm; R^0_{ps} then starts to decrease, but it rises again at $d=110$ nm.

have R^0_{ps} over 80% in wavelengths from 550 to 800 nm. The simulation condition is at normal incidence $\theta=0°$ with $\phi=45°$, and the permittivity dispersion of silver is obtained from polynomial fitting to the experimental data (no source specified in the reference). Here we use the same grating profile but with the permittivity dispersion from [31] to do the calculation.

The result is represented by the solid square curve in Fig. 5, which is very close to the result shown in Fig. 4 in [8], with a slight difference in the short wavelength region. The $R^0_{ps}(\lambda)$ in this visible spectrum shows a higher value in the long wavelength end than in the short.

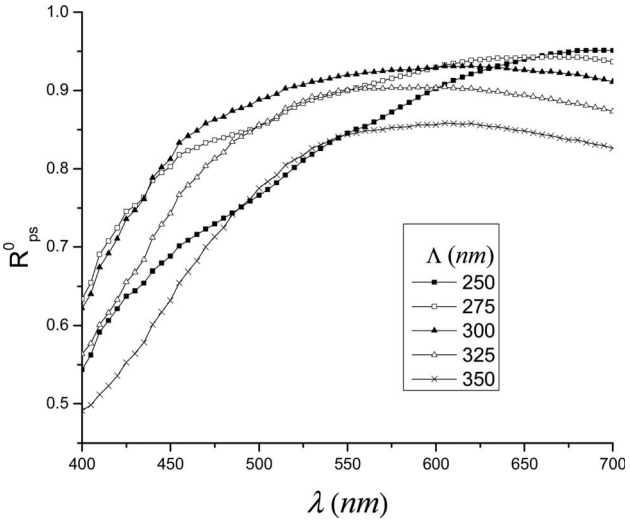

Fig. 5. Broadband $R^0_{ps}(\lambda)$ curves of a silver Gaussian-ridge grating of 50 nm width (FWHM), 240 nm height, and grating pitch Λ varying from 250 nm to 350 nm. The simulation condition is at normal incidence with $\phi=45°$ and the permittivity dispersion of silver obtained from polynomial fitting to experimental data. The peak of $R^0_{ps}(\lambda)$ is moving toward the center of visible spectrum as the Λ increases. The curve of solid squares of $\Lambda=250$ nm is consistent with the result in [8].

In considering the application to polarizing illumination devices, such as LCDs [32], it would be favorable if the peak of $R^0_{ps}(\lambda)$ were more centered in the visible spectrum. Here we investigate this possibility by slight tuning of the pitch of the Gaussian-ridge grating with only slight change in $R^0_{ps}(\lambda)$. We see in Fig. 5 that the $R^0_{ps}(\lambda)$ peak moves toward the center of spectrum by gradually increasing the pitch while keeping the same height and FWHM. However, note that the $R^0_{ps}(\lambda)$ will drop off if the pitch increases too much, say to 350 nm, as indicated by the curve of crosses in Fig. 5.

Although the Gaussian-ridge-shape grating has manifested high R^0_{ps} value, in practice it is not easy to fabricate such a narrow profile due to its high aspect ratio and need for precise control of the Gaussian shape. Here we suggest two other specific configurations of grating that also fulfill the same broadband R^0_{ps} performance that was shown in Fig. 1(b). One is a symmetric trapezoidal grating of 60 nm top, 70 nm bottom, 124 nm height, and 197 nm period. The other is a rectangular grating with its width 56 nm, height 110 nm, and period 160 nm. Both preserve high broadband polarization conversion. For detailed discussion of achromatic R^0_{ps} of rectangular gratings with different aspect ratios and metals, readers can consult [10]. Also, in the case of asymmetric trapezoidal metallic gratings, the R^0_{ps} of monochromatic waves with different inclination angles is discussed in [33].

With the same incident conditions and permittivity dispersion used in Fig. 5, the three broadband R^0_{ps} curves of the above-mentioned grating profiles are shown in Fig. 6. All of these R^0_{ps}s are above 80% in wavelengths from near 450 to 650 nm, which demonstrates the high performance of broadband PC. Here the pitch of a Gaussian-ridge grating is 310 nm, chosen to be more centered in the visible spectrum. Another issue is that for wide-angle application instead of normal incidence, we should explore the broadband R^0_{ps} with arbitrary polar angle θ.

Before discussing any numerical work, we briefly review here the analysis of the optimized azimuthal condi-

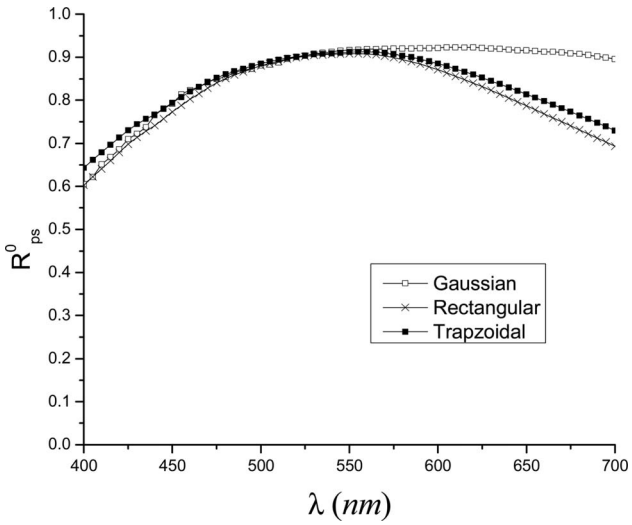

Fig. 6. Performance of broadband $R^0_{ps}(\lambda)$ for the three grating profiles in Fig. 1(b) with the same simulation conditions as Fig. 5; the pitch of the Gaussian-ridge grating is $\Lambda=310$ nm, chosen to be more centered in the visible spectrum.

tion of R_{ps}^0. For quite a long time, it has been understood that in one propagation direction of a surface plasmon wave, the peak of plasmon resonance occurs at $\phi=45°$ along one branch of resonance curves for conical diffraction gratings [2,34]. Later, it was pointed out in [20] that in the same propagation direction of surface plasmon wave, there exist two branches of resonance. Both branches exhibit local maxima of PC.

This is indicated in Figs. 7(a)–7(d) along two $R_{ps}^0(\theta,\phi)$ branches of resonance curves calculated by RCWA for shallow sinusoidal gratings. Again, these figures are consistent with the results reported in [20,21]. In Fig. 7(a), the first branch is the dominant set with maximum $R_{ps}^0=1.74\%$ at $(\theta,\phi)=(2.7°,45°)$; the second set has its maximum $R_{ps}^0=0.96\%$ at $(\theta,\phi)=(53.75°,66°)$.

For such shallow gratings, the first branch R_{ps}^0 follows the square rule of a sinusoidal function, $R_{ps}^0(\theta,\phi) \propto \sin^2(2\phi)$, which has been both empirically and analytically proven [1,21]. So it is natural to expect that the maximum R_{ps}^0 will occur at $\phi=45°$. However, for deep-

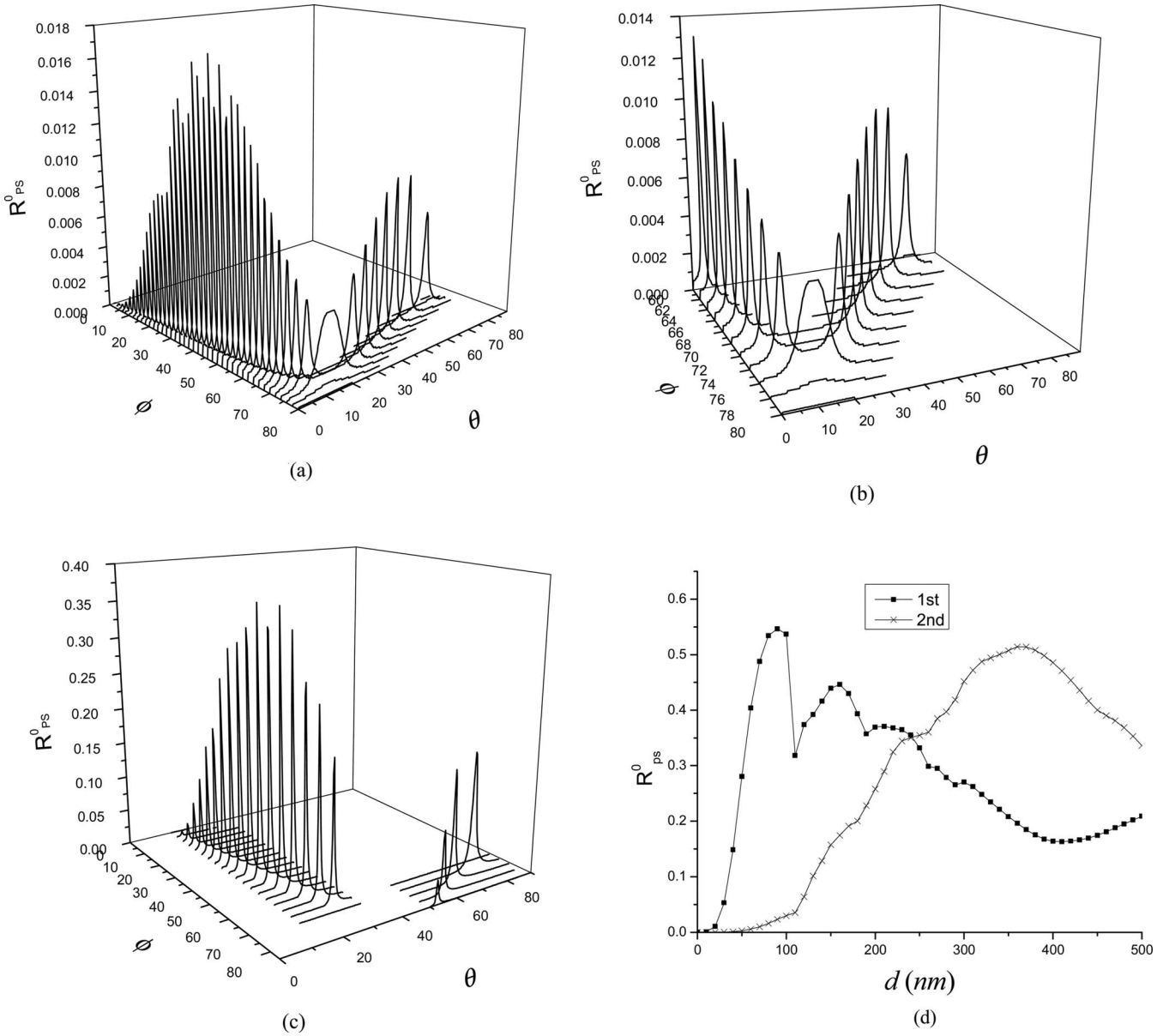

Fig. 7. (a) Two $R_{ps}^0(\theta,\phi)$ branches of resonance curves for a shallow sinusoidal grating of $\varepsilon=-8.23+0.29i$, $\Lambda=575.27$ nm, $d=11.5$ nm, and $\lambda=632.8$ nm. The first branch is the dominant set with maximum $R_{ps}^0=1.74\%$ at $(\theta,\phi)=(2.75°,45°)$, and the second set has its maximum $R_{ps}^0=0.96\%$ at $(\theta,\phi)=(53.75°,66°)$. (b) The major region of second-branch resonance in (a) within the ϕ range from 60° to 80°. (c) Two $R_{ps}^0(\theta,\phi)$ branches of resonance curves for the grating profile in Fig. 2. (d) The two R_{ps}^0 curves with increasing depth d in (c). The curve of squares is the first resonance branch with $(\theta,\phi)=(21°,45°)$, and that of crosses is the second branch with $(\theta,\phi)=(76.5°,74°)$. The R_{ps}^0 of the second branch is larger than that of the first branch when $d>0.27\Lambda$ (230 nm).

groove gratings, the other branch can become dominant as the groove depth increases. This is shown in Fig. 7(d) when $d>0.27\Lambda$: the R_{ps}^0 at $\phi=74°$ in the second branch is larger than that at $\phi=45°$ in the first branch. We would emphasize here that with increasing grating depth, other resonance branches may appear and the maximum R_{ps}^0 is not necessarily located in these two branches.

Now, for broadband incident waves we need a high-aspect-ratio grating with $d>\Lambda$, or at least $d\approx\Lambda$, to achieve high R_{ps}^0. In this case, the interaction of light and surface plasmon is even more complicated. The R_{ps}^0 depends on the details of both how the surface plasmon wave is coupled into photons (optical modes) and how these photons interfere with the diffracted light. The coupling depends critically on the groove configuration, and these excited optical modes can have self-interferences inside the groove and even across to adjacent grooves. One example is that in a subwavelength grating the surface plasmon wave forms a standing wave in a narrow groove [35].

Furthermore, the dispersion of surface plasmon waves may constitute complex band gap structures [36]. What is more, the large excitation of surface plasmon light does not guarantee high R_{ps}^0 value, for it may destructively interfere with itself, dissipating energy into uncoupled waves, or undergo extra phase delay that causes the con-

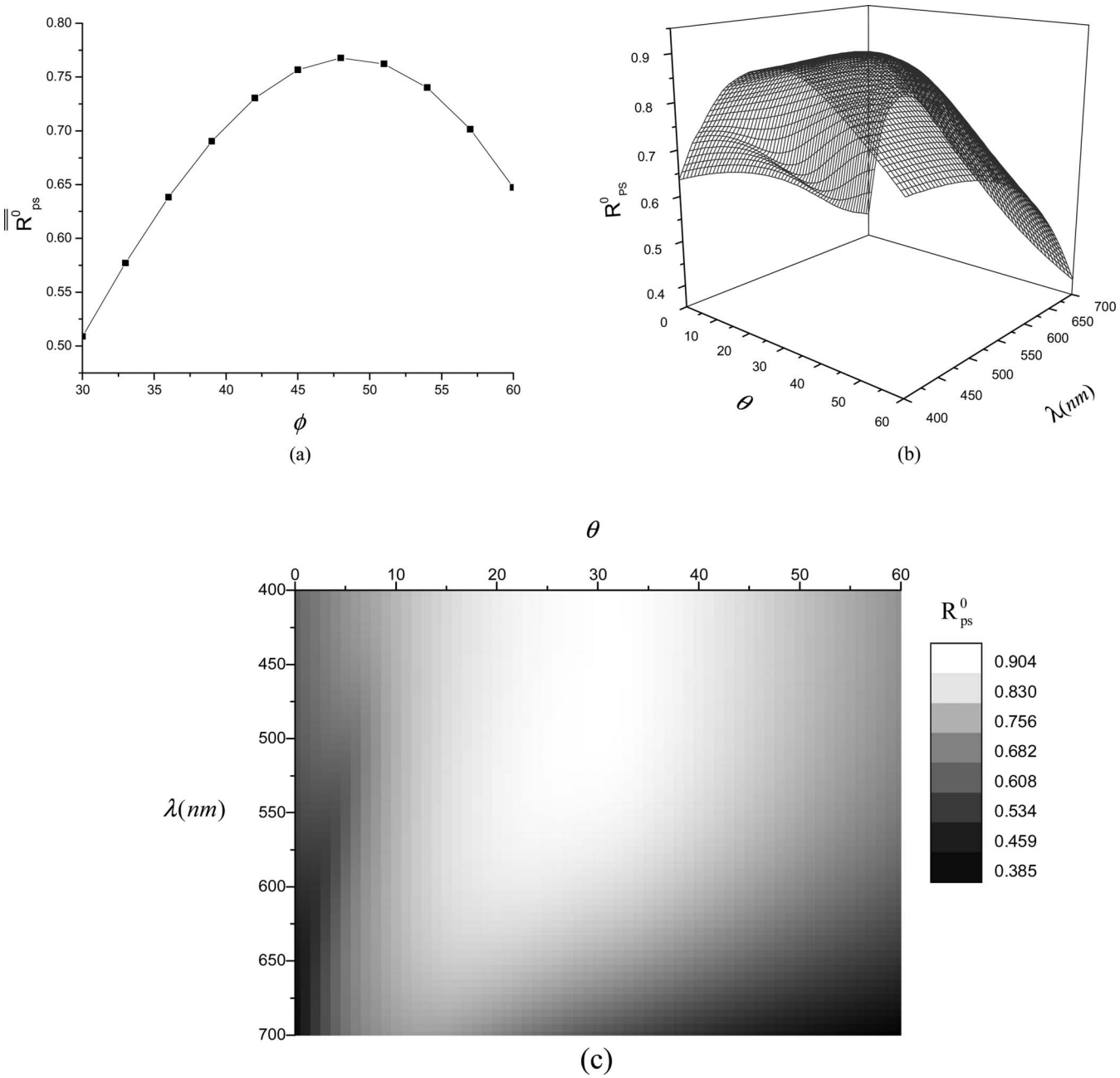

Fig. 8. (a) Average broadband polarization conversion efficiency $\overline{\overline{R_{ps}^0}}(\phi)$ over θ and λ of the trapezoidal grating profile in Fig. 1(b), with the ϕ ranging from 30° to 60°. The peak of $\overline{\overline{R_{ps}^0}}(\phi)$ is 84.5% at $\phi=48°$. (b) The $R_{ps}(\theta,\lambda)$ diagram of $\phi=48°$ in (a), which is over 80% in most regions of (θ,λ) with the maximum $R_{ps}^0(30°,650)=90\%$ and the minimum $R_{ps}^0(60°,450)=38\%$. (c) Top view of (b).

verted polarization to rotate an additional $\pi/2$ back to the original polarization. Thus, R_{ps}^0 cannot be treated by the simple two-branch analysis mentioned above. All these mechanisms will affect the maximum R_{ps}^0, especially when we consider large incidence angle θ. Therefore, there is no reason to expect the overall optimized azimuthal angles should occur at $\phi=45°$.

Here we define a figure of merit, the average PC efficiency $\overline{\overline{R_{ps}^0}}(\phi)$ over θ and λ with fixed ϕ as

$$\overline{\overline{R_{ps}^0}}(\phi) = \frac{\int\int R_{ps}^0(\theta,\lambda)\mathrm{d}\theta\mathrm{d}\lambda}{\Delta\theta\Delta\lambda}, \tag{14}$$

where $\Delta\theta$ and $\Delta\lambda$ are the integral intervals of polar angle and wavelength, respectively. Figure 8(a) shows the $\overline{\overline{R_{ps}^0}}(\phi)$ curve from $\phi=30°$ to $\phi=60°$ for the subwavelength trapezoidal grating in Fig. 1(b). As we can see, the maximum $\overline{\overline{R_{ps}^0}}(\phi)$ is 84.5%, occurring at $\phi=48°$. Figure 8(b) illustrates the $R_{ps}^0(\theta,\lambda)$ diagrams of $\phi=48°$, which demonstrate that the $R_{ps}^0(\theta,\lambda)$ can reach over 80% in most of the range of (θ,λ), with the maximum value $R_{ps}^0(30°,650)=90\%$ and the minimum $R_{ps}^0(60°,450)=38\%$. Figure 8(c) is the top view of Fig. 8(b).

All these numerical results show that it is possible to have both broad and wide-angle PC with subwavelength metallic gratings. Moreover, due to the complicated entanglement between the excited surface plasmon wave and reflected light, we expect these simulations can provide more information toward theoretical modeling or fundamental analysis of the optimized conditions for R_{ps}^0.

4. SUMMARY

RCWA is widely employed in the community of calculation of diffraction gratings. In this paper, we demonstrate again that the conical RCWA can accurately determine PC through metallic gratings, as the results of various examples given here are in agreement with those previously calculated by Chandezon's method or obtained by experiment. PC depends on the details of plasmons excited on the metal surface. Since the surface plasmon wave equation itself is derived from the Maxwell equation [37] and also satisfies the periodic boundary condition of gratings, it is natural that RCWA can calculate the total $\boldsymbol{E}$, $\boldsymbol{H}$ fields caused by surface plasmon and reflected light. The phenomenon of resonance and absorption can also be treated by RCWA, because the mutual coupling of many Floquet waves, including the evanescent modes, are all contained in the RCWA formulation.

We have investigated three metallic gratings that enable the performance of broadband wide-angle PC. The optimized R_{ps}^0 with azimuthal angle ϕ is discussed in detail; it is not necessarily at 45° as in the case of normal incidence. Moreover, the subwavelength grating acts like a PC mirror, as it satisfies Snell's law. This characteristic increases the applicability of such polarization rotating devices. The reciprocity relation of R_{ps}^0 makes it convenient that we can choose the incident light to be either p- or s-polarized waves.

Other grating profiles may be found that have equivalent or better performance not even limited to single-surface-layer gratings. However, the coupling situation between the surface plasmons and light inside the grating groove would be more complicated. This needs more future studies, and the required numerical analysis can be accomplished by RCWA, as we have shown in this paper.

ACKNOWLEDGMENT

The authors are indebted to Chi-Mei Optoelectronics (Taiwan) for financial support.

REFERENCES

1. G. P. Bryan-Brown and J. R. Sambles, "Polarization conversion through the excitation of surface plasmons on a metallic grating," J. Mol. Spectrosc. **37**, 1227–1232 (1990).
2. S. J. Elston, G. P. Bryan-Brown, T. W. Preist, and J. R. Sambles, "Surface-resonance polarization conversion mediated by broken surface symmetry," Phys. Rev. B **44**, 3483–3485 (1991).
3. Y.-L. Kok and N. C. Gallagher, "Relative phases of electromagnetic waves diffracted by a perfectly conducting rectangular-grooved grating," J. Opt. Soc. Am. A **5**, 65–73 (1988).
4. C. W. Haggans, L. Li, T. Fujita, and R. K. Kostuk, "Lamellar gratings as polarization components for specularly reflected beams," J. Mol. Spectrosc. **40**, 675–686 (1993).
5. S. R. Seshadri, "Polarization conversion by reflection in a thin-film grating," J. Opt. Soc. Am. A **18**, 1765–1776 (2001).
6. I. R. Hooper and J. R. Sambles, "Surface plasmon polaritons on narrow-ridged short-pitch metal gratings in the conical mount," J. Opt. Soc. Am. A **20**, 836–843 (2003).
7. A. V. Kats, M. L. Nesterov, and A. Yu. Nikitin, "Polarization properties of a periodically-modulated metal film in regions of anomalous optical transparency," Phys. Rev. B **72**, 193405 (2005).
8. I. R. Hooper and J. R. Sambles, "Broadband polarization-converting mirror for the visible region of the spectrum," Opt. Lett. **27**, 2152–2154 (2002).
9. B. T. Hallam, C. R. Lawrence, I. R. Hooper, and J. R. Sambles, "Broad-band polarization conversion from a finite periodic structure in the microwave regime," Appl. Phys. Lett. **84**, 849–851 (2004).
10. N. Passilly, K. Ventola, P. Karvinen, P. Laakkonen, J. Turunen, and J. Tervo, "Polarization conversion in conical diffraction by metallic and dielectric subwavelength gratings," Appl. Opt. **46**, 4258–4265 (2007).
11. J. Chandezon, M. T. Dupuis, G. Cornet, and D. Maystre, "Multicoated gratings - a differential formalism applicable in the entire optical region," J. Opt. Soc. Am. **72**, 839–846 (1982).
12. Y. Okuno, "The mode-matching method," in *Analysis Methods for Electromagnetic Wave Problems*, E. Yamashita, ed. (Artech House, 1990), pp. 107–138.
13. Y. Okuno and T. Suyama, "Numerical analysis of surface plasmons excited on a thin metal grating," J. Zhejiang Univ., Sci. **7**, 55–70 (2006).
14. T. Suyama, Y. Okuno, and T. Matsuda, "Enhancement of TM-TE mode conversion caused by excitation of surface plasmons on a metal grating and its application for refractive index measurement," Electromagn. Waves **72**, 91–103 (2007).
15. M. G. Moharam, E. B. Grann, D. A. Pommet, and T. K. Gaylord, "Formulation for stable and efficient implementation of the rigorous coupled-wave analysis of binary gratings," J. Opt. Soc. Am. A **12**, 1068–1076 (1995).
16. M. G. Moharam, D. A. Pommet, E. B. Grann, and T. K. Gaylord, "Stable implementation of the rigorous coupled-wave analysis for surface-relief gratings: enhanced

transmittance matrix approach," J. Opt. Soc. Am. A **12**, 1077–1086 (1995).
17. L. Li, "A modal analysis of lamellar diffraction gratings in conical mountings," J. Mol. Spectrosc. **40**, 553–573 (1993).
18. P. C. Logofatu, S. A. Coulombe, B. K. Minhas, and J. R. McNeil, "Identity of the cross-reflection coefficients for symmetric surface-relief gratings," J. Opt. Soc. Am. A **16**, 1108–1114 (1999).
19. D.-E. Yi, Y.-B. Yan, H.-T. Liu, S. Lu, and G.-F. Jin, "Broadband achromatic phase retarder by subwavelength grating," Opt. Commun. **227**, 49–55 (2003).
20. R. A. Depine and M. Lester, "Internal symmetries gratings in conical diffraction from metallic gratings," J. Mol. Spectrosc. **48**, 1405–1411 (2001).
21. A. V. Kats and I. S. Spevak, "Analytical theory of resonance diffraction and transformation of light polarization," Phys. Rev. B **65**, 195406 (2002).
22. R. Petit, *Electromagnetic Theory of Gratings* (Springer-Verlag, 1980).
23. L. Li and C. W. Haggans, "Convergence of the coupled-wave method for metallic lamellar diffraction gratings," J. Opt. Soc. Am. A **10**, 1184–1189 (1993).
24. P. Lalanne and G. M. Morris, "Highly improved convergence of the coupled-wave method for TM polarization," J. Opt. Soc. Am. A **13**, 779–784 (1996).
25. G. Granet and B. Guizal, "Efficient implementation of the coupled-wave method for metallic lamellar gratings in TM polarization," J. Opt. Soc. Am. A **13**, 1019–1023 (1996).
26. P. Lalanne, "Convergence performance of the coupled-wave and the differential methods for thin gratings," J. Opt. Soc. Am. A **14**, 1583–1591 (1997).
27. E. Popov and M. Nevière, "Maxwell equations in Fourier space: fast-converging formulation for diffraction by arbitrary shaped, periodic, anisotropic media," J. Opt. Soc. Am. A **18**, 2886–2895 (2001).
28. L. Li, "Use of Fourier series in the analysis of discontinuous periodic structures," J. Opt. Soc. Am. A **13**, 1870–1876 (1996).
29. C. C. Tsai and S. T. Wu, are preparing a manuscript to be called "Fast convergence formulation of rigorous coupled-wave analysis for surface relief gratings".
30. R. A. Depine and C. I. Valencia, "Reciprocity relations for s-p polarization conversion," Opt. Commun. **117**, 223–227 (1995).
31. E. D. Palik, *Handbook of Optical Constants* (Academic, 1997).
32. D. K. Yang and S. T. Wu, *Fundamentals of Liquid Crystal Devices* (Wiley, 2006).
33. R. A. Depine and M. E. Inchaussandague, "Polarization conversion from highly conducting, asymmetric trapezoidal gratings," Appl. Opt. **42**, 3742–3744 (2003).
34. T. Inagaki, M. Motosuga, K. Yamamori, and E. T. Arakawa, "Photoacoustic study of plasmon resonance absorption in a diffraction grating," Phys. Rev. B **28**, 1740–1744 (1983).
35. M. B. Sobnack, W. C. Tan, N. P. Wanstall, T. W. Preist, and J. R. Sambles, "Stationary surface plasmons on a zero-order metal grating," Phys. Rev. Lett. **80**, 5667–5670 (1998).
36. W. C. Tan, T. W. Preist, J. R. Sambles, and N. P. Wanstall, "Flat surface-plasmon-polariton bands and resonant optical absorption on short-pitch metal gratings," Phys. Rev. B **59**, 12661–12666 (1999).
37. H. Raether, *Surface Plasmons* (Springer-Verlag, 1988).